AIMS Materials Science, 3(3): 737-755.
DOI: 10.3934/matersci.2016.3.737
Received: 18 March 2016
Accepted: 21 June 2016
Published: 28 June 2016

http://www.aimspress.com/journal/Materials

Research article

Inorganic alkali lead iodide semiconducting $APbI_3$ (A = Li, Na, K, Cs) and NH_4PbI_3 films prepared from solution: Structure, morphology, and electronic structure

Lucangelo Dimesso *, Michael Wussler, Thomas Mayer, Eric Mankel, and Wolfram Jaegermann

Materials Science Department, Technische Universitaet Darmstadt, Jovanka-Bontschits-Strasse 2, D-64287, Darmstadt, Germany

* **Correspondence:** Email: ldimesso@surface.tu-darmstadt.de; Tel: +49-6151-16-20779; Fax: +49-6151-16-20771.

Abstract: $APbI_3$ alkali lead iodides were prepared from aqueous (A= Na, Cs, ammonium NH_4^+, and methylammonium $CH_3NH_3^+$) and acetone (A= Li, K) solutions by a self-organization low temperature process. Diffraction analysis revealed that the methylammonium-containing system ($MAPbI_3$) crystallizes into a tetragonal perovskite structure, whereas the alkali and NH_4^+ systems adopt orthorhombic structures. Morphological inspection confirmed the influence of the cation on the growth mechanism: for A = Cs and NH_4^+, needle-like crystallites with lengths up to 3–4 mm; for A = K, thin stripes with lengths up to 5–6 mm; and for A = MA^+, dodecahedral crystallites were observed. For A = Li and Na, the $APbI_3$ systems typically resulted in polycrystalline aggregates. Optical absorption measurements demonstrated large energy band gaps for the alkali and ammonium systems with values between 2.19 and 2.40 eV. For electronic and chemical characterization by photoelectron spectroscopy, the as-prepared powders were dissolved in di-methylformamide and re-crystallized as thin films on F:SnO_2 substrates by spin-coating. The binding energy differences between Pb4f and I3d core levels are highly similar in the investigated systems and close to the value measured for PbI_2, indicating similar relative partial charges and formal oxidation states. The binding energies of the alkali ions are in accordance with oxidation state +1. The X-ray excited valence band spectra of the investigated $APbI_3$ systems exhibited similar line shapes in the region between the valence band maximum and 4.5 eV higher binding energy due to common PbI_6 octahedra which dominate the electronic structure. While the ionization energy values are quite similar (6.15 ± 0.25 eV), the Fermi-level positions of the unintentionally doped materials vary for different cations

and different batches of the same material, which indicates that the position of the Fermi level can be influenced by changing the process parameters.

Keywords: solution process; alkali lead iodide; ammonium lead iodide; X-ray photoelectron spectroscopy; ultra-violet photoelectron spectroscopy

Abbreviations

MAI	Methylammonium iodide
FTO	Fluor-doped tin oxide glass substrate
XRD	X-ray diffraction analysis
SEM	Scanning electron microscopy
DMF	N,N-dimethylformamide
XPS	X-ray photoelectron spectroscopy
UPS	Ultraviolet photoelectron spectroscopy
RPM	Rotations per minute
VB	Valence band
WF	Work function
E_B	Binding energy

1. Introduction

Group 14 halometalates of the composition AMX_3 represent a large group of semiconducting materials. In these compounds, MX_6 octahedra form one-dimensional (1D) edge-sharing or three-dimensional (3D) corner-sharing (perovskite) structures. The formation of a defined polymorph depends on preparation method and temperature [1,2]. The valence band of such semiconductors primarily stems from the X^- halogen anion fully occupied valence *p*-orbitals and the conduction band from the empty M^{2+} metal cation valence *p*-orbitals, while the uppermost occupied and lowest unoccupied states of the A^+ cation are off the band edges [3]. Thus, the variation of the A species does not directly influence the energy gap, but may influence it indirectly by acting on the MX_6 configuration in the lattice. For $RbPbI_3$ and $CsPbI_3$ band structures, calculations show increased dispersion in the 3D phase that leads to a smaller band gap as compared to the 1D-phase. Organic-inorganic iodide perovskites, such as $CH_3NH_3PbI_3$, have recently drawn attention [4–7] due to functional qualities as light-absorbers in solar cells, achieving average rates of 15% [8–11] and certified rates up to 20% [10]. As for the cause of some of the $MAPbI_3$ electronic peculiarities, the methyl-ammonium ion (MA) with its dipole moment has been previously examined [11]. The contribution of the inorganic counterparts also deserves proper investigation. Assessments of Alkali-PbI_3 systems have shown energy gaps in the optical spectrum, suggesting an advantageous role as photovoltaic absorbers. While the perovskite phase (3D) of $CsPbI_3$ is black with a band gap around 1.67 eV, [12] the 1D-phases are yellow with energy gaps above 2 eV and may also be potentially suitable for photovoltaic applications, e.g., in tandem cell configurations or as luminescence materials.

Perovskites have been the subject of great interest for many years, due to the large number of compounds which crystallize in this structure. Many studies have been published on the substances with the formula AMX_3, such as $BaTiO_3$, $NaNbO_3$ and $CsPbCl_3$ [13,14]. Besides these inorganic perovskites, various amines may be placed on the A-site, such as ammonium (NH_4^+) [15], methylammonium ($CH_3NH_3^+$) [16,17,18], and formamidinium ($NH_2CH{=}NH_2^+$) [19,20]. These organic cations are particularly common in compounds based around lead and tin halides. In these compounds, the perovskite aristotype is a cubic *Pm3m* framework structure of composition AMX_3, where A (Wyckoff position 1a) is commonly a large cation coordinated to 12X (3c) anions, M (1b) is a smaller metal bonded to six X anions, and MX_6 octahedra are corner-connected to form a three-dimensional framework. The hinged octahedra allow for wide adjustment of the M–X–M bond angle, and several sets of cooperative rotations, known as tilt transitions, promote symmetry reduction of the aristotype [21]. The black phase of $CsPbI_3$ can be grown as nanoparticles in a high-temperature solution process using a boiling solvent [22], whereas the low-temperature aqueous solution process applied in the current study leads to growth of the yellow modification in needle-shaped crystals in accordance with the 1D-arrangement of the PbI_6 octahedra [23].

The main purpose of our work targets the synthesis and characterization of $APbI_3$ compounds with systematically varied A cations from the alkali series and the organic ammonium cation NH_4^+ in comparison to the well studied $CH_3NH_3PbI_3$ using a modified simple self-organizing solution based-method. The crystallographic (XRD), morphologic (SEM), and optical properties were measured on the primary $APbI_3$ systems. In addition, thin films were prepared from solutions of the primary materials dissolved in dimethylformamide (DMF) and photoelectron-spectroscopically characterized using XPS and UPS. Basic semiconductor properties such as energy gap, work functions, and absolute ionization energies have been derived.

2. Materials and Method

$APbI_3$ materials were prepared by a self-organization process, using precursor solutions that were prepared by commercially available compounds. In particular, LiI (lithium iodide), NaI (sodium iodide), KI (potassium iodide), NH_4I (ammonium iodide), $Pb(CH_3COO)_2{*}2H_2O$ (lead acetate dihydrate), HI (47% wt., iodic acid stabilized with 1.5% wt. hypophosphorous acid), and CsI (cesium iodide) were used as delivered by Alfa Aesar without further purification. Tri-halogeno-plumbates (II) with potassium, ammonium, and cesium were synthesized through a modified self-organization process, as previously reported [16]. The materials were prepared in a concentrated aqueous solution of iodic acid at 110 °C, which contained Pb^{2+} ions [from lead (II) acetate] and a respective amount of cesium, potassium, or ammonium-iodide.

The methylammonium-containing system was prepared with a respective amount of $CH_3NH_3^+$ (by adding a 40% solution of CH_3NH_2 in water) [16,24]. As these perovskites are grown from aqueous solutions, crystallization water is to be expected [25]. For A = Na and Li, severe preparation conditions such as concentrated and hot alkaline solutions are necessary in order to obtain high yields of pure products. Moreover, the complex liquid-solid equilibrium in the solutions requires very careful control of the NaI (or LiI)/PbI_2 starting stoichiometry. Therefore, lithium- and sodium-containing tri-iodo-plumbates were prepared by adding the corresponding amount of PbI_2 to solutions containing lithium and sodium ions from LiI and NaI, respectively, in acetone at 40 °C, in which both salts are soluble. The microcrystalline precipitates formed spontaneously while cooling to

room temperature, subsequently separated by filtration, and dried at room temperature in air. Finally, the materials were stored in a glove-box under inert atmosphere to minimize reactions with ambient atmosphere, particularly moisture.

The structural analysis was performed by X-ray powder diffraction (XRD) on thoroughly grinded samples using a D8 Bruker powder diffractometer (Cu $K\alpha_1$ + Cu $K\alpha_2$ radiation) with a *theta / 2 theta* Bragg-Brentano configuration. The diffractometer is equipped with an Energy Dispersion Detector Si(Li) to minimize fluorescence effects. A scanning electron microscope (SEM) Philips XL 30 FEG was used to investigate the morphology of the samples.

Optical diffuse-reflectance measurements were performed on the prepared powders using a Perkin Elmer UV/VIS/NIR double-monochromator spectrometer operating from 200 to 2500 nm. $BaSO_4$ was used as a non-absorbing reflectance reference. The generated reflectance-versus-wavelength data were used to estimate the band gap of the material by converting reflectance to absorbance data, according to the Kubelka−Munk equation: $\alpha/S = (1- R)^2/2R$, where R is the reflectance and α and S are the absorption and scattering coefficients, respectively [26,27].

For X-ray and ultra-violet photoelectron spectroscopy (XPS and UPS), the primary synthesized crystals were grinded, dissolved in dimethylformamide (33% wt), recrystallized from a spin-coated (in air) liquid layer on a transparent conductive oxide FTO (fluorine doped SnO_2) on glass substrates (Pilkington TEC15), and dried at 80 °C. The reference system $MAPbI_3$ was deposited in a two-step process. In the first step, a 37% wt solution of PbI_2 was spin-coated at 1000 RPM and dried at 90 °C for 30 min. In the second step, the PbI_2 films were dipped in an alcoholic solution (2-propanol) of MAI (10mg/ml), then rinsed with 2-propanol and finally dried out at 90 °C for 30 min. The films were stored in a glove box under dry atmosphere (<5ppm water). All photoemission spectra were collected under a pressure of 10^{-9} mbar and in normal emission. The spectrometer (Phi Versaprobe II) was calibrated to the Fermi-edge of a silver reference and the $Ag3d_{5/2}$ core level at a binding energy E_B = 368.26 eV. To perform XPS measurements, a monochromatic AlKα X-ray-gun with an excitation energy of 1486.6 eV was used, and the pass energy of the hemispherical analyzer was set to 11.5 eV. In addition to the emissions of the examined species, Sn and oxygen emissions were also observed, due to partial coverage of the FTO substrate and residuals of the solvent. A helium gas discharge lamp was used to generate He-I (21.22 eV) for UPS measurements. As the UPS valence band (VB) spectra show structures due to incompletely covered FTO, the valence band spectra were also taken with AlKα XPS excitation, for which the relative cross section for orbitals of lead and iodine, which form the valence band, are pronounced compared to UV excitation [54]. As the FTO work function (WF) is larger than the observed WF, the onset of the secondary electrons is initiated by secondary electrons emitted from the film, which occurs on incompletely covered FTO substrates, as well. Thus, the WFs are derived from the secondary electron emission onset in He-I spectra taken with an applied bias voltage of 3 eV between the substrate and the spectrometer. All measurements were performed at room temperature. Chemical states and electronic states (valence band maximum position, work function, and ionization potential) of the samples were derived.

3. Results and Discussion

The primary crystalline powders were prepared using a self-organizing process from solution; the details of this process have been previously reported [24]. Crystallographic stability and probable structure of perovskites can be deduced by considering the (*t*) (Goldschmidt's tolerance factor) and

(μ) (Li's octahedral factor) factors [28]. The tolerance factor evaluates ionic size mismatches of the perovskite-structure until a different structure-type is formed in the perovskite AMX_3. The evaluation methods of the tolerance factors t and μ have been discussed in the Supporting Information of Ref. [28]. The values of t factors have been summarized in Table 1 in order of the ionic radii [29]. Analysis of Table 1 indicated that the Cs-containing system fulfills the conditions for a perovskite structured material (for halide-containing systems, the lowest value is 0.813), whereas the ammonium-containing compound may lead to distorted perovskites [28]. Below ~0.80, other structures, such as the ilmenite-type ($FeTiO_3$), are more stable due to the similar sizes of the cations A and M. The materials formed from aqueous solution, for which crystallization occurs by cooling slowly from 100–110 °C to room temperature without stirring, show discrete needle-like structures when A= Cs, K, and NH_4^+, in contrast to polyhedral structures for $CH_3NH_3^+$, shown in Figure 1A–D. The A = Li and Na based materials grown from acetone solution form polycrystalline aggregates, as clearly shown in Figure 1E and Figure 1F, respectively. The morphological investigation of the $APbI_3$ systems, shown in Figure 1A–D, revealed that, for A = Cs, the crystallites generally grow as narrow platelets with lengths up to 3–4 mm, which is a typical crystal habit of an orthorhombic lattice (space group *Pnma*) (Figure 1A). A similar habit can be observed in the ammonium-containing system, as shown in Figure 1C; on the other hand, the crystallites for A = K demonstrated a thin stripe-like structure (Figure 1B) with lengths up to 5–6 mm, which is a typical crystalline habit of a tetragonal lattice. Finally, unlike the alkaline metals and ammonium-containing compounds, for A = MA, the formation and growth of dodecahedral crystallites (Figure 1D) were observed (space group *I 4/mcm*).

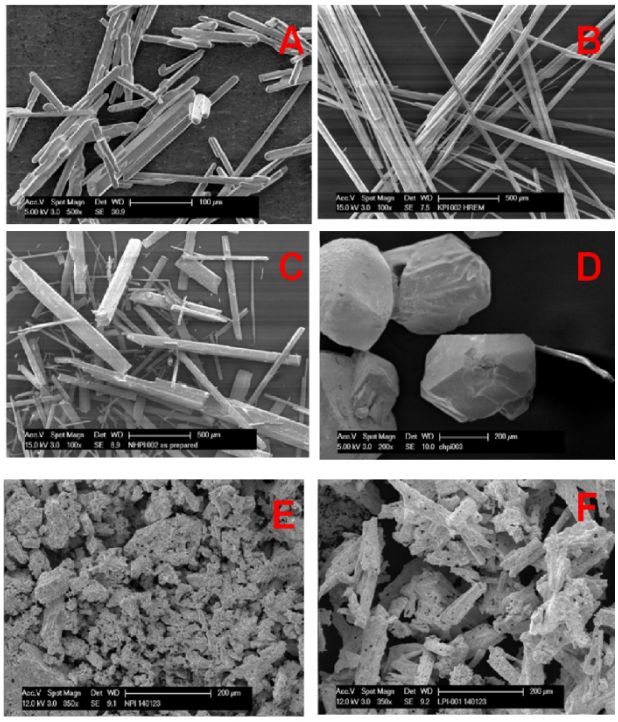

Figure 1. Typical SEM images exhibit the crystal habits of the respective $APbI_3$ compounds, obtained from the self-organizing method from aqueous solutions with A) A = Cs, B) A = K, C) A = NH_4^+, D) A = MA^+ and from acetone solutions with E) A = Na and F) A = Li, respectively.

Table 1. Summary of the values *t* for the $APbI_3$ systems. The octahedral factor (μ) is 0.541 for all considered systems (Ref. [28]).

A	Ionic radius (Å)*	*t*
**CH_3NH_3	1.80	0.912
Cs	1.78	0.830
NH_4	1.61	0.795
K	1.38	0.747
Na	1.02	0.672
Li	0.76	0.618

*Ref. [29]. Coordination number: 6, State: high spin, Cs coordination number: 9;
**Ref. [28]. For the ionic radii of Pb and I, 1.19 Å and 2.20 Å were used, respectively.

The powder XRD analysis confirmed the crystal structures initially drawn from SEM images. The X-ray diffractograms of the perovskites grown from aqueous solution, i.e., systems containing Cs, K, NH_4^+, and $CH_3NH_3^+$, are shown in Figure 2A–F. For Cs, K, and NH_4^+, the room temperature crystalline reflections can be indexed on the basis of an orthorhombic structure (space group *Pnma*), by comparison to the data presented previously by Trots [30] and Bedlivy [31]. Upon evaporation or cooling of the solutions, $APbI_3 \cdot nH_2O$ is obtained, where *A* = Li, Na, K, NH_4, Rb, or Cs and *n* = 0, 2, 4, or 6, depending on the alkali ion and on the conditions of formation [32 and references there in]. Of this family, only the structures of the two isotopic anhydrous salts $RbPbI_3$ and low temperature $CsPbI_3$ phases are known. On the other hand, Fan [32] recently reported the preparation of anhydrous NH_4PbI_3 by solid-state reaction in a sealed and evacuated quartz tube. The obtained prism-shaped yellow crystals were used to determine the crystalline structure and properties of the system. In the ammonium-containing system, the XRD-patterns suggest the presence of reflections due to secondary phase(s) (indicated with * in Figure 2B). Although all systems crystallize as orthorhombic structures, the intensity differences resulting from the same diffractions can be explained by the different crystalline habits of the specimens, which are influenced by thermodynamic and kinetic factors during the formation and growth of the crystallites. For $A = MA^+$ (Figure 2D), the crystalline reflections indicate the formation of a tetragonal structure at room temperature (space group *I 4/m or I 4/mcm*), i.e., a 3D perovskite structure [16]. Zieger [33] reported an attempt to obtain the Na-containing compound by the interaction of an aqueous NaI solution (conc. 1 g ml^{-1}) with PbI_2, which was dissolved in the solution up to saturation. After drying out, a pale yellow hygroscopic powder was obtained. The diffraction pattern revealed the presence of unreacted precursors PbI_2, NaI, and a new phase ($NaPbI_3$). Very similar results were obtained experimentally, and by comparing the results of the XRD analysis, we find similar reflections of an additional crystalline phase, indicated by asterisks in Figure 2E. This phase can be identified as $NaPbI_3 \cdot xH_2O$ (the content of water was not measured), in which x can tend to 4 or even 6 for NaI : PbI_2 = 50:50 (mol/mol), as reported by Roger [34], when exposed to high relative humidity (ca. 60%) for several days. A similar argument can be used to explain the data in the Li-containing system. Similarly, the formation of $LiPbI_3 \cdot 4H_2O$ as solid phase in LiI concentrated aqueous solutions (≅ 60% wt.) has been reported [27]. In our case, the presence of this phase as well as the presence of unreacted PbI_2 and LiI have been confirmed (Figure 2F) by comparison to data previously reported [35,36]. Indeed, for A = Li, detailed reports of crystalline structure could not be found in the literature. Consequently, we cannot attribute any Miller

indexes to XRD patterns in Figure 2F. For better analysis, we improved the visual representation of the XRD patterns by enlarging Figures 2A–2F and reporting them in Figures S2–S4 of the Supplementary Information. The Li-containing material is highly hygroscopic even at low relative humidity, thus, storage under inert atmosphere is mandatory.

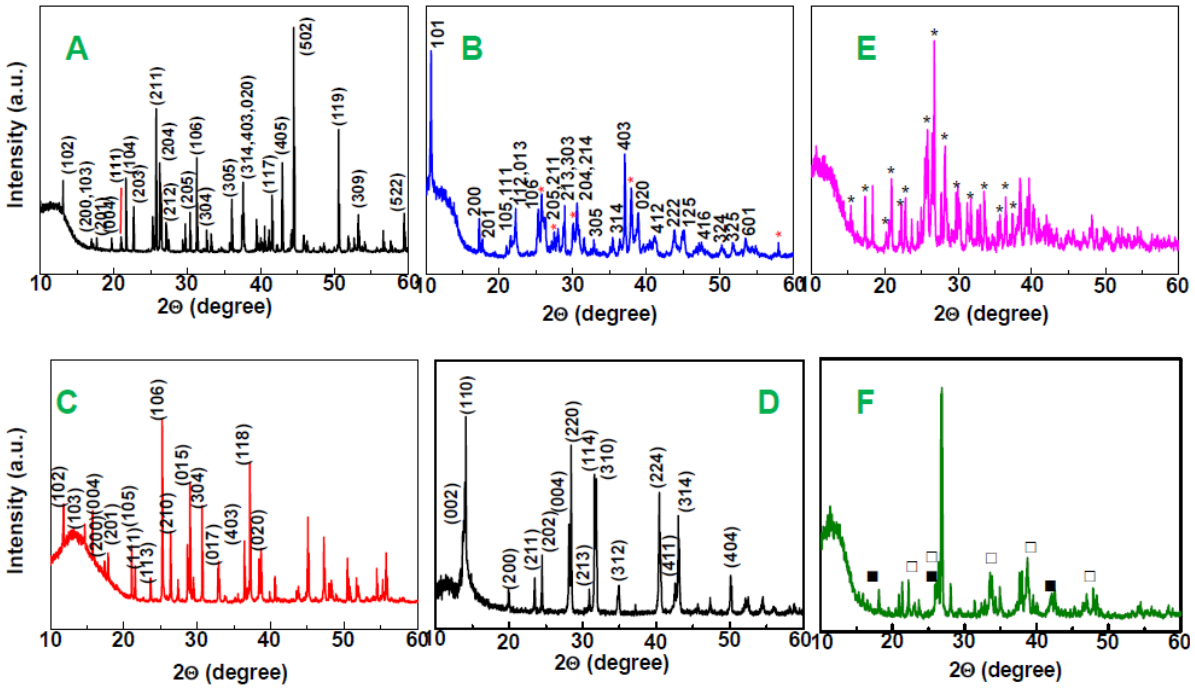

Figure 2. XRD-patterns of the $APbI_3$ for A) A = Cs, B) A = NH_4^+, C) A = K, D) = MA^+, E) A = Na, and F) A = Li. Secondary phases are indicated as not identified (*), unreacted PbI_2 (□), and non-reacted LiI (■), respectively.

Both structural and morphological features can dramatically influence the physical properties of the prepared materials. The optical absorption spectra of the $APbI_3$ systems are displayed in Figure 3 and the corresponding Tauc plots (explained below) in Figure 4. The main optical absorption is attributed to electron excitations from the valence band to the conduction band. The values of the band-gaps are given by the absorption edge, obtained by fitting the linear part of the absorbance spectrum [37]. The values of the band-gaps have been summarized in Table 1 in the order of the ionic radii [29]. Data of PbI_2 without any further cations are added for comparison and are in accordance with published data [1,38]. The relationship between the absorption coefficient (α) near the absorption edge and the optical band gap (E_g) approximately obeys the following formula [39,40]

$$\alpha = A(h\nu - E_g)^n/h\nu \qquad (\text{Eq. 1})$$

where A is a parameter that relates to the effective masses associated with the valence and conduction bands, $h\nu$ is the photon energy, and n is related to the nature of the fundamental optical transition, i.e., for direct allowed transitions n = ½, while for indirect allowed transitions n = 2 [41]. Assuming direct transitions, the value of the energy gaps are obtained by extrapolating the linear section of $(\alpha h\nu)^2$ to α = 0, as shown in the Tauc plots in Figure 4. The respective values for the energy gaps are also reported in Table 2.

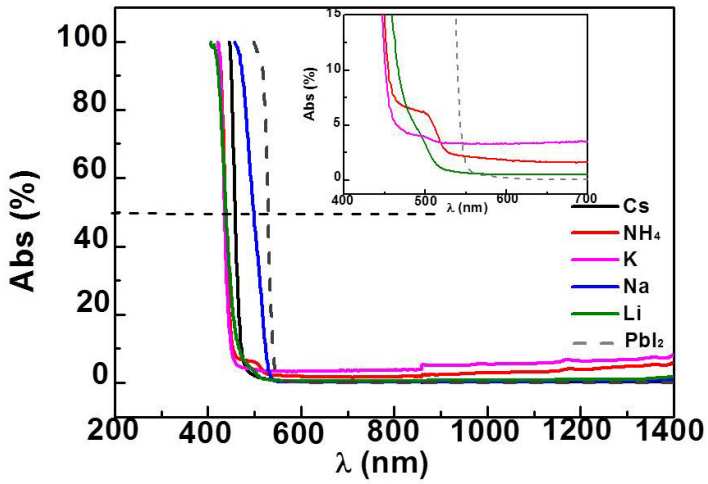

Figure 3. Normalized optical spectra of the synthesized $APbI_3$ systems measured at room temperature. The systems with NH_4^+, K, and Li show a small step at longer wavelength (inset), which is attributed to the presence of PbI_2 phase.

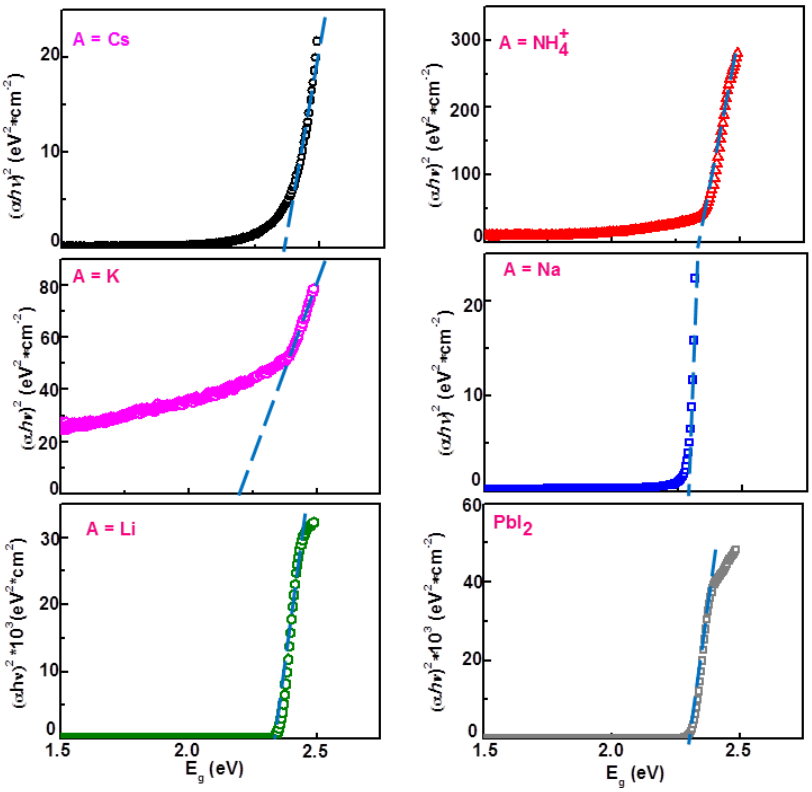

Figure 4. Assuming direct transitions, the band gaps E_g are obtained from $(\alpha h\nu)^2$ (or Tauc) plots for the $APbI_3$ systems by extrapolation to $\alpha = 0$. The data are reported in Table 2.

Table 2. Band gap energy values for the $APbI_3$ systems obtained from a) the data shown in Figure 3 (by using λ_{onset} obtained by fitting the linear part of the absorbance spectra, b) from the Tauc plots shown in Figure 4 and c) published in the literature. (v. n. m.: value not measured; v. n. f.: value not found).

A	Ionic radius (Å)*	λ_{onset} (nm)	E_g (eV)[a]	E_g (eV)[b]	E_g (eV)[c]	Ref.
**CH_3NH_3	1.80	816	1.52	1.53	1.54	44
Cs	1.78	476	2.60	2.40	2.76	42
NH_4	1.61	465	2.67	2.37	2.32	-
K	1.38	458	2.71	2.19	2.60	46
Na	1.02	530	2.34	2.30	v.n.m.	47
Li	0.76	486	2.55	2.36	v.n.f.	-
PbI_2	-	554	2.24	2.32	2.301 ± 0.038	38

*Ref. [29]. Coordination number: 6, State: high spin, Cs coordination number: 9; **Ref. [24].

Several important points are to note. The energy band gap values for $CsPbI_3$ in Table 2 are lower than those reported by Clark [42] (E_g = 2.76 eV) for samples obtained by cooling melts containing the appropriate proportions of CsI and anhydrous PbI_2. $CsPbI_3$ is a well known and thoroughly investigated perovskite system; its orthorhombic lattice (space group *Pnma*) with a three-dimensional network. The orthorhombic lattice is retained up to temperatures of 563–602 K; at higher temperatures, it turns into cubic phase ((red arrow) according to previous data), whereas monoclinic phase occurs upon temperature decreases ((blue arrow) according to later detailed studies [30]) Cubic ← Tetragonal ← Orthorhombic → Monoclinic. The higher energy band gap values have been explained with the formation and growth of Cs_4PbI_6 as secondary phase because the two compounds have very similar melting points [42,44].

Potassium-containing perovskites crystallize as $KPbI_3 \cdot 2H_2O$ solid phase with an octahedral crystalline structure (space group *Pnma*) and form thin flexible pale-yellow needles. An investigation of the phase diagram from solutions was already carried out by Talmadge [45]. Salau [46] investigated the optical absorption properties at room temperature of PbI_2-KI thin films prepared by crystals that were subsequently crushed into powders and used for evaporation purposes. Assuming a direct energy gap, calculations suggest (eq.1) E_g values of 2.32 eV for PbI_2 and 2.4 eV for $KPbI_3$, which are higher than the values obtained (2.19 eV) following preparation in aqueous solutions (Table 2).

Na-Pb-I systems, with a very low Pb content (with 10^{-3} in weight), may be functionally used as phosphors; Baltog [47] reported a dependence of the luminescence properties as a function of Pb-content in the system. The introduction of Pb induced the formation of impurity aggregation. When the amount of the impurity aggregation reaches a critical concentration, the aggregation gives birth to a precipitation phase of the type PbI_2:*n*NaI. Consequently, an exciton-like emission appears in the luminescence spectrum with a corresponding shift of the absorption peak to a wavelength value above 500 nm, as confirmed by our absorption data and direct band gap model (Figure 4D).

Unlike Cs- and K-containing systems, NH_4^+-, Na-, and Li-containing systems have been poorly investigated as possible materials for solar cells. The ammonium-containing system ($NH_4PbI_3 \cdot 2H_2O$) crystallizes in space group *Pnma* as well [31,32], and forms thin pale yellow needles. The crystals

are very similar to anhydrous $CsPbI_3$, the only obvious difference being the pronounced yellow color of the latter [32]. $NH_4PbI_3{\cdot}2H_2O$ is iso-structural to $KPbI_3{\cdot}2H_2O$ and demonstrates only minor differences in bond lengths and angles. The structures contain $[PbI_3^-]$ double chains of edge-sharing PbI_6 octahedra; the repeat periods of the $[PbI_3^-]$ chains and, consequently, certain I-Pb-I angles, vary considerably with the alkali ion. Since the alkali ions have their shortest distances parallel to the chain directions, the repulsion between them, which increases with the size of the ions, is most likely responsible for this effect. The anion chain has no significant hydrogen-bonding interactions with the cations. Previously only poorly investigated, the optical absorption properties of the $NH_4PbI_3{\cdot}2H_2O$ system have now been examined experimentally and are reported in Table 2. Recently, Filip [48] obtained a band gap of 1.9 eV for the NH_4PbI_3 system by using the single particle Green's function G and the screened Coulomb interaction W (GW method) and Wannier functions to calculate the quasiparticle band gaps, band structures, and effective masses of lead iodide perovskites. The different band gap values may be explained by the crystalline structure of the material, as influenced by the presence of water during preparation.

The powder XRD diffractogram of the Li-Pb-I system revealed the formation of $LiPbI_3{\cdot}nH_2O$ (water content was not determined), but some PbI_2 remained unreacted under the current experimental conditions. This may explain the very similar profiles of the Tauc plots as well as the slight difference between the values of the optical energy gaps (2.32 eV and 2.36 eV for PbI_2 and $LiPbI_3{\cdot}nH_2O$, respectively), as presented in Table 2. The collected data also illuminate novel properties of the $LiPbI_3{\cdot}4H_2O$ system, detailed in Table 2. Notably, the optical energy gap value and the XRD pattern in Figure 2F (enlarged in Figure S4, even with secondary phases) represent the first reported measurements for the Li-containing lead iodide system. Further analysis remains to be done to contribute to a deeper understanding of these systems.

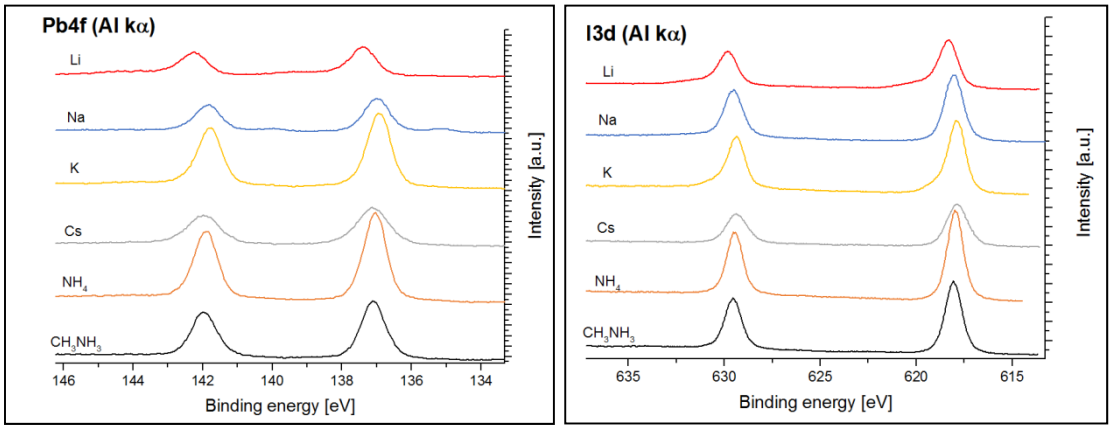

Figure 5. XPS core level spectra of A) Pb4f and B) I3d for the synthesized $APbI_3$ systems (excitation energy: 1486.6 eV). Binding energies (E_B) are given with respect to the valence band maximum of the respective compound.

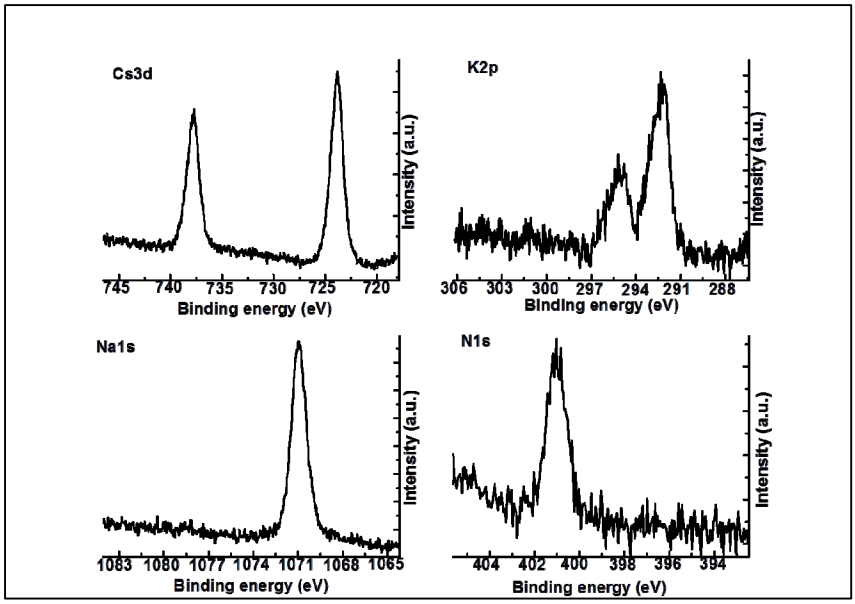

Figure 6. XPS core level spectra of the cations A in the synthesized $APbI_3$ systems. A) Cs3d, B) K2p, C) Na1s, and D) N1s of NH_4^+ (excitation energy: 1486.6 eV). Binding energies are given with respect to the valence band maximum of the compound with the respective cation A.

Table 3. Values of iodine/lead and alkaline metal/lead atomic ratios obtained from XPS measurements. Photoelectron emissions of $I3d_{7/2}$, Pb4f, Na1s, K2p, $Cs3d_{5/2}$, N1s, and C1s have been used.

A	I/Pb (atomic ratio)	A/Pb (atomic ratio)
Li	3.7	Not resolvable
Na	4.3	2.7
K	2.7	0.7
Cs	2.4	0.9
NH_4	2.7	0.4
CH_3NH_3	3	C=0.8/N=0.7
Stoichiometry in solution	3	1

Furthermore, the electronic structure of these materials as thin films in photoemission spectroscopy were studied. The films were prepared by dissolving the synthesized powder in di-methyl-formamide (DMF), spin-coating on FTO coated glass substrates, and heating at T = 80 °C for a few minutes in air. During the evaporation of the solvent, re-crystallization of the corresponding $APbI_3$ phase took place on the substrates. This was confirmed by the XRD analysis and optical

measurements of the $APbI_3$-layers, as shown in Figure S1A and Figure S1B for the $MAPbI_3$ system. Indeed, the crystalline reflections of the deposited layer (Figure S1B) match the reflections of the starting powder (S1A). The higher intensity can be explained by higher crystallinity of the recrystallized material. For quantitative evaluation of the stoichiometry in these films, the most intense photoelectron line of every element was applied [49]. Detailed Pb4f and I3d XPS core level spectra are shown in Figure 5A and Figure 5B, respectively, while the core level spectra of the cations (Cs 3d, K 2p, Na 1s and N 1s) [52] are displayed in Figure 6.

The relative atomic concentrations were calculated from the integrated photoemission intensities using the atomic sensitivity factors according to Wagner and machine-specific parameters [52]. The spectral backgrounds were subtracted using a Tougaard-type function [50]. The Li1s photoelectron emission is very weak and, because of the overlap with the I4d emission line, the Li1s photoemission line could not be resolved. Besides the expected elements of the films tin, oxygen, and carbon, photoelectron lines were also detected. Tin and, in part, oxygen originate from the FTO-coating of the substrate due to imperfect coverage of the studied film. Oxygen may, in addition, stem from surface phases formed through interaction with humidity, whereas carbon may be introduced from ubiquitously adsorbed hydrocarbons in the atmosphere during preparation at ambient atmosphere. The results of the measured chemical compositions are summarized in Table 3. The experimental values of I/Pb and A/Pb atomic ratios in the $APbI_3$ thin films differ from the stoichiometry compositions of I/Pb = 3:1 and A/Pb = 1/1 used in solution. For I : Pb < 3 and A : Pb < 1 molar ratios, the presence of PbI_2 occurs as an additional phase, whereas for I : Pb > 3 and A : Pb > 1 ratios, the presence of A-iodide may be assumed. This could be explained by supposing that the fast evaporation of the solvent changes the thermodynamic and/or kinetic conditions of the crystallization process of the $APbI_3$ phases on the substrate, which favor secondary processes like formation of secondary phases.

In photoemission spectroscopy, the Fermi level is intrinsically used as the reference energy. As the Fermi level was found at slightly varied positions for individual samples of the same material, the core level spectra in Figure 5 and Figure 6 are displayed with respect to the valence band maximum for better comparison. On the other hand, the valence band spectra and the secondary edges displayed in Figure 7 are in reference to the Fermi level of the respective sample to illustrate the respective doping level. $MAPbI_3$ consistently displays a typical *n*-type behavior across all batches, whereas the materials with Cs, K, and NH_4^+ demonstrate weak p-type and those with Na and Li present strong *n*-type behavior. According to these different positions of the Fermi level, it seems possible to shift the position of the Fermi level in the band gap by changing the process parameters, particularly the stoichiometry. Emara [51] found a relationship between the stoichiometry and the position of the Fermi level in $MAPbI_3$ system. The authors reported a wide variety of ionization energies, ranging from 5.67 to 6.4 eV due to changes in film preparation and film stoichiometry.

Moreover, Miller [56] and Schulz [57] reported independently that the position of the Fermi level energy can be influenced by the nature of the substrate even by depositing thick layers of $MAPbI_3$. In order to minimize the influence of the substrate, all samples have been deposited on F:SnO2-layered glass substrates. XRD measurements confirm that the excess material is incorporated not as secondary phases but rather as interstitials incorporated into the perovskite structure, without showing additional diffraction patterns. Such interstitials and variations in composition can be assumed to be the reason for the widely differing values of ionization energies and perovskite device efficiencies reported in the literature. The core level binding energy values are

listed in Table 4. The Pb4f doublet spectra show the $Pb4f_{7/2}$ emission around 137 eV below the respective valence band edge. The spin orbit splitting of 4.87 eV is in agreement with the value in literature of 4.86 eV [52]. The measured binding energies E_B confirm that the lead ions are in ionization state +2 [53] as expected for the $APbI_3$ systems; however, weak emissions shifted to lower binding energies have been observed for the Na- and Li-containing systems (135 eV and 140 eV, respectively), tentatively attributed to elemental lead (Pb^0) and Pb^{4+}, respectively. Although the growth and the effects of Pb^0 are not completely understood, its presence can be explained by the exposure to moisture, as reported by Lindblad [49] for $CH_3NH_3PbI_3$, and also thermic decomposition by formation of lead clusters [58]. In the Li compound, a weak and broad emission doublet at 2.4 eV higher binding energy is observed. This emission is assigned to a shake-up satellite due to excitation of an electron from the valence to the conduction band in the process of emitting the Pb4f photoelectrons. The binding energy of the $I3d_{5/2}$ and $I3d_{3/2}$ states are 618 eV and 629.5 eV, respectively, indicating an oxidation state of (−1). The splitting is independent of the respective cation A and with 11.50 eV close to standard values for iodine ions [52]. In the Li-system, weak, broad side emissions at 2.2 eV higher binding energy are found, similarly attributed to shake-up satellites of the I3d photoelectrons, as observed for the Pb4f emission in this system. The binding energy differences between $Pb4f_{7/2}$ and $I3d_{5/2}$ (Table 3) are very similar (481 eV), indicating that the partial charges of Pb and I are nearly independent on the respective cation A. The XPS spectra of the alkaline metal ions are shown in Figure 6. Due to spin-orbit coupling, the XPS spectra show two emission lines (doublet) for Cs3d and K2p and one emission line (singlet) for Na1s and N1s. Furthermore, all cations reveal valence state +1, as expected [53]. On the other hand, the photoelectron emission of Li1s (at 56 eV) is much weaker by a factor of about 100 than that of $I4d_{3/2}$ (51 eV); for this reason, a resolution of the Li1s photoelectron emission in the XPS spectra could not be performed and analyzed.

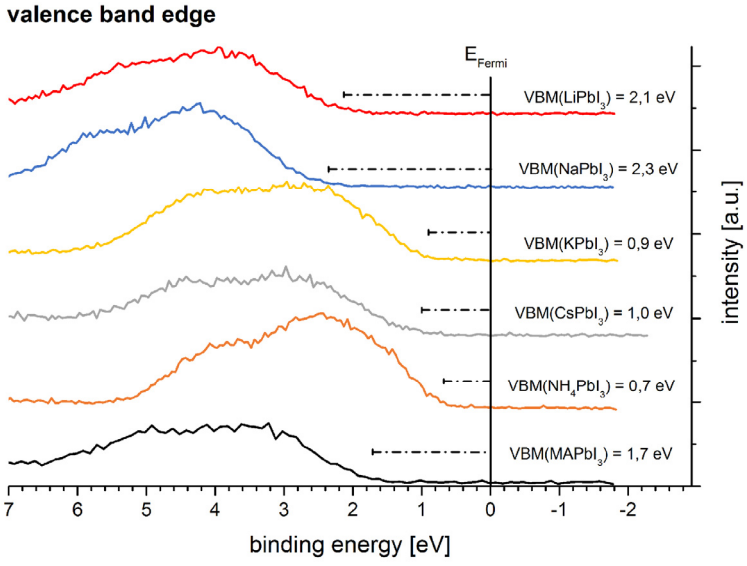

Figure 7. XPS valence band spectra for the synthesized systems with the respective cation A, as indicated in the figure. The binding energies are given with respect to the Fermi level of the respective sample.

The XPS valence band spectra are displayed in Figure 7. The line shape of the upper valence

bands is quite similar, and their width is about 4.5 eV. These states are formed mostly by the iodide 5p orbitals and in minor content of Pb6s states of the PbI_6 octahedra [55], which also explains the constant energy distance of the iodine core level with respect to the valence band maximum. For $CH_3NH_3PbI_3$, it is known from calculation and IPES measurements that the PbI_6 octahedra are responsible for the valence band and the conduction band [57,59]. The band gap is primarily dependent on the orientation of these octahedra to each other [1]: face- and edge-sharing materials (as PbI_2) have a band gap >2 eV, while corner-sharing materials, such as $CH_3NH_3PbI_3$ or $CsPbI_3$, have a smaller band gap <2 eV. Unfortunately, it was impossible to resolve the structure to such a level to confidently conclude the electronic structure.

Table 4. Pb4f, I3d, alkali metal ion, or N1s XPS core level binding energies with reference to the valence band maximum of the respective $APbI_3$ system.

A	E_B Pb4f$_{7/2}$ (eV)	E_B I3d$_{5/2}$ (eV)	E_B cation (eV)	E_B I3d$_{5/2}$ – E_B Pb4f$_{7/2}$ (eV)
CH_3NH_3	137.11	618.07	400.82 (N1s)	480.96
NH_4	137.06	617.96	401.05 (N1s)	480.90
Cs	137.11	617.87	723.34 (Cs3d$_{5/2}$)	480.76
K	136.95	617.97	292.38 (K2p$_{3/2}$)	481.02
Na	136.98	618.03	1070.72 (Na1s)	481.05
Li	137.37	618.30	-	480.93

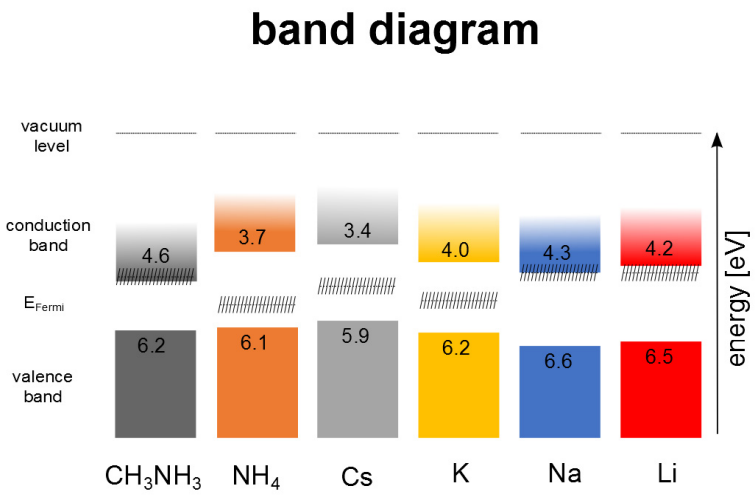

Figure 8. Band edges of the synthesized systems, as derived from the XPS valence band spectra measurements for different cations. For the energy gaps, the values from absorption measurements (Table 3) are used. The varied (unintentionally) doping levels in different batches are indicated by a hatched region for the Fermi level position.

The work functions were measured via the secondary electron edge by He(I) excitation energy (21.22 eV). Studies [59,60] which determined the band gap for $CH_3NH_3PbI_3$ found a slightly higher band gap (1.7 eV) if IPES/UPS is used compared to optical measurements and EQE measurements (1.5–1.6 eV); a similar behavior may also be observed for the alkali systems. But, the studied

materials are direct semiconductors as the Tauc-plots confirm. Therefore the band gaps, determined by the optical measurements are reliable and were used to draw the band structure. The measured values are summarized in Figure 8. While the ionization energy values are quite similar (6.15 ± 0.25 eV), the work function varies due to variation in the Fermi-level positions of the unintentionally doped materials for different cations and different batches with the same cation. These first data suggest that *p*-type systems can be prepared for NH_4, Cs, and K, and n-type for Na and Li.

4. Conclusions

This work presents an investigation of layers of $APbI_3$ systems (A = alkali metals, ammonium, methylammonium (MA^+) (as reference)) prepared by self-organization processes from solution at low temperature. The morphological analysis revealed the influence of the respective cation on the crystalline habit of the materials. For A = Cs and NH_4^+, the crystallites generally demonstrated needle-like morphology with lengths up to 3–4 mm, whereas for A = K, they exhibited a thin stripe-like structure with lengths up to 5–6 mm. On the other hand, the crystallites of $MAPbI_3$ generally formed dodecahedra, which is a typical crystalline habit of a body-centered tetragonal lattice. By decreasing the ionic radius, the $APbI_3$ systems tend to form polycrystalline aggregates, such as in the sodium- and lithium-containing systems. In the X-ray diffractograms, the crystalline reflections were indexed on the basis of an orthorhombic structure (space group *Pnma*), whereas for A = MA^+, the crystalline reflections indicate the formation of a tetragonal structure at room temperature (space group *I 4/m or I 4/mcm*).

Optical absorption measurements on the primary synthesized materials indicate that Cs-, NH_4-, K-, and Na-containing systems behave like direct-gap semiconductors with energy band gaps ranging between 2.19 eV and 2.40 eV at room temperature. As the energy gap is determined mainly by the PbI_6 octahedra and their crystal structure, common to all investigated systems (except the $MAPbI_3$), the similar values of the energy band gaps are related to a minor effect of the cation A on the valence and conduction band structure. The XPS spectra show the iodine and lead ions in formal oxidation state −1 in +2, respectively. As the $Pb4f_{7/2}$ $I3d_{5/2}$ binding energy differences are very similar (481 eV), the partial charges of Pb and I are only weakly dependent on the respective cation A. All cations A are in +1 oxidation state. The valence bands measured with X-ray excitation show very similar line shapes from the valence band maximum (VBM) to 4.5 eV below, in agreement with common PbI_6 octahedra in the investigated systems. The ionization energies are around 6.1 ± 0.2 eV; unintentionally doped films formed from dissolved primary synthesized materials show degenerate n-type for the A = MA, strong n-type for A = Na and Li, and weak p-type for A = NH_4, Cs, and K.

This work investigated the structural, microstructural, optical, and electronic features of $APbI_3$ systems with different positive monovalent cations “A”, which were prepared under very similar conditions. According to our results, the positive cations begin to influence system properties as early as the preparation of the materials.

Acknowledgements

The Authors thank the Federal Ministry of Research and Development (BMBF) for the financial support during this work. Many thanks are due to Mr. J.-C. Jaud for the technical assistance in the XRD analysis and Mrs. C. Spanheimer for the technical assistance in the SEM analysis. Also thanks

to Julianne McCall for editing the manuscript.

Conflict of Interest

The authors declare that there is no conflict of interest regarding the publication of this manuscript.

References

1. Papavassiliou GC (1997) Three- and low-dimensional inorganic semiconductors. *Prog Solid St Chem* 25: 125–270.
2. Billing DG, Lemmerer A (2009) Inorganic-organic hybrid materials incorporating primary cyclic ammonium cations: The lead bromide and chloride series. *Cryst Eng Comm* 11: 1549–1562.
3. Brgoch J, Lehner AJ, Chabinyc M (2014) Ab initio calculations of band gaps and absolute band positions of polymorphs of $RbPbI_3$ and $CsPbI_3$: Implications for main-group halide perovskite photovoltaics. *J Phys Chem C* 118: 27721–27727.
4. Baibarac M, Preda N, Mihut L (2004) On the optical properties of micro- and nanometric size PbI_2 particles. *J Phys Condens Matter* 16: 2345–2356.
5. Stranks SD, Eperon GE, Grancini G (2013) Electron-hole diffusion lengths exceeding 1 micrometer in an organometal trihalide perovskite absorber. *Science* 342: 341–344.
6. Xing G, Mathews N, Sun S (2013) Long-range balanced electron- and hole-transport lengths in organic-inorganic $CH_3NH_3PbI_3$. *Science* 342: 344–347.
7. Frost JM, Butler KT, Brivio F (2014) Atomistic origins of high-performance in hybrid halide perovskite solar cells. *Nano Lett* 14: 2584–2590.
8. Du MH (2014) Efficient carrier transport in halide perovskites: theoretical perspectives. *J Mater Chem A* 2: 9091–9098.
9. Burschka J, Pellet N, Moon SJ (2013) Sequential deposition as a route to high-performance perovskite-sensitized solar cells. *Nature* 499: 316–319.
10. Yang WS, Noh JH, Jeon NJ (2015) High-performance photovoltaic perovskite layers fabricated through intramolecular exchange. *Science* 348: 1234–1237.
11. Oxton IA, Knop O, Duncan JL (1977) The Infrared Spectrum and Force Field of the Methylammonium ion in $(CH_3NH_3)_2PtCl_6$. *J Mol Struct* 38: 25–32.
12. Chung I, Song JH, Im J (2012) $CsSnI_3$: Semiconductor or Metal? High electrical conductivity and strong Near-Infrared Photoluminescence from a single material. High hole mobility and phase-transitions. *J Am Chem Soc* 134: 8579–8587.
13. Shirane G, Yamada Y (1969) Lattice-dynamical study of the 110K phase transition in $SrTiO_3$. *Phys Rev* 177: 858–863.
14. Prokert F (1981) Neutron Scattering Studies on phase transitions and phonon dispersion in $CsSrCl_3$. *Phys Status Solidi (b)* 104: 261–265.
15. Rubin J, Palacios E, Bartolome J, et al. (1995) A single-crystal neutron diffraction study of NH_4MnF_3. *J Phys Condens Matter* 7: 563–575.
16. Poglitsch A, Weber D (1987) Dynamic disorder in methylammoniumtrihalogenoplumbates (II) observed by millimeter-wave spectroscopy. *J Chem Phys* 87: 6373–6378.

17. Knop O, Wasylishem RE, White M (1990) Alkylammonium lead halides. Part2. $CH_3NH_3PbX_3$ (X = C1, Br, I) perovskites: cuboctahedral halide cages with isotropic cation reorientation. *Can J Chem* 68: 412–422.
18. Swainson IP, Hammond RP, Soulliere C (2003) Phase transitions in the perovskite methylammonium lead bromide, $CH_3ND_3PbBr_3$. *J Solid State Chem* 176: 97–104.
19. Mitzi DB, Liang K (1997) Synthesis, resistivity, and thermal properties of the cubic perovskite $NH_2CH{=}NH_2SnI_3$ and related systems. *J Solid State Chem* 134: 376–381.
20. Lee Y, Mitzi DB, Barnes PW (2003) Pressure-induced phase transitions and templating effect in three-dimensional organic-inorganic hybrid perovskites. *Phys Rev B* 68: 366–369.
21. Baikie T, Fang Y, Kadro JM (2013) Synthesis and crystal chemistry of the hybrid perovskite $(CH_3NH_3)PbI_3$ for solid-state sensitised solar cell applications. *J Mater Chem A* 1: 5628–5641.
22. Protesescu L, Yakunin S, Bodnarchuk MI (2015) Nanocrystals of cesium lead halide perovskites ($CsPbX_3$, X = Cl, Br, and I): Novel optoelectronic materials showing bright emission with wide color gamut. *Nano Lett* 15: 3692–3696.
23. Shum K, Chen Z, Qureshi J (2010) Synthesis and characterization of $CsSnI_3$ thin films. *Appl Phys Lett* 96: 221903.
24. Dimesso L, Dimamay M, Hamburger M (2014) Properties of $CH_3NH_3PbX_3$ (X = I, Br, Cl) powders as precursors for organic/inorganic solar cells. *Chem Mater* 26: 6762–6770.
25. Wells LH (1893) Über die Cäsium- und Kalium-Blei halogenide. *Z anorg Chemie* 3: 195–210.
26. Kortüm G, Braun W, Herzog G (1963) Prinzip und Meßmethodik der diffusen Reflexionsspektroskopie. *Angew Chem* 75: 653–661.
27. McCarthy TJ, Tanzer TA, Kanatzidis MG (1995) A new metastable three-dimensional bismuth sulfide with large tunnels: Synthesis, structural characterization, ion-exchange properties, and reactivity of KBi_3S_5. *J Am Chem Soc* 117: 1294–1301.
28. Dimesso L, Quintilla A, Kim YM (2015) Investigation of formamidinium and guanidinium lead tri-iodide powders as precursors for solar cells. *Mater Sci Eng B* 204: 27–33.
29. Shannon RD (1976) Revised effective ionic radii and systematic studies of interatomic distances in halides and chalcogenides. *Acta Crystallogr* A 32: 751–767.
30. Trots DM, Myagkota SV (2008) High-temperature structural evolution of caesium and rubidium triiodoplumbates. *J Phys Chem Solids* 69: 2520–2526.
31. Bedlivy D, Mereiter K (1980) The structure of potassium lead triiodide dihydrate and ammonium Lead Triiodide Dyhydrate. *Acta Cryst* B 36: 782–785.
32. Fan LQ, Wu JH (2007) (IUCr) Poly[diaquatris([mu]4-isophthalato)dilanthanum(III)]. *Acta Cryst* E 63: 189.
33. Ziger E, Kukol' V, Babich G (1980) New three-component compounds based on alkali metal, Lead and Bismuth Iodides. *Russ J Inorg Chem (Engl Transl)* 25: 1201–1203.
34. Roger M (1944) Abstract of Engineer Doctor Work (Paris).
35. Condeles JF, Lofrano RCZ, Rosolen JM (2006) Stoichiometry, surface and structural characterization of Lead Iodide thin films. *Brazilian J Phys* 36: 320–323.
36. Chihara H, Kawakami T, Soda G (1969) The NMR study of the disorder in Lithium Iodide Monohydrate and Monodeuterate. *J Magn Res* 1: 75–88.
37. Ghobadi N (2013) Band gap determination using absorption spectrum fitting procedure. *Inter Nano Lett* 3: 2.

38. Ferreira da Silva A, Veissid N, An CY (1996) Optical determination of the direct band gap energy of lead iodide crystals. *Appl Phys Lett* 69: 1930–1932.
39. Salvador P (1982) Analysis of the physical properties of TiO_2-Be electrodes in the photoassisted oxidation of qater. *Sol En Mater* 6: 241–250.
40. Tsunekawa S, Fukuda T, Kasuya A (2000) Blue shift in ultraviolet absorption spectra of monodisperse CeO_{2-x} nanoparticles. *J Appl Phys* 87: 1318–1321.
41. Tauc J (1968) Optical properties and electronic structure of amorphous Ge and Si. *Mater Res Bull* 3: 37–46.
42. Clark SJ, Donaldson JD, Harvey JA (1995) Evidence for the direct population of solid-state bands by nonbonding electron pairs in compounds of the type CsM"X, (MI' = Ge, Sn, Pb; X = CI, Br, I). *J Mater Chem* 5: 1813–1818.
43. Moller CK (1958) Crystal structure and photoconductivity of Caesium Plumbohalides. *Nature* 182: 1436.
44. Stoumpos CC, Malliakas CD, Kanatzidis MG (2013) Semiconducting Tin and Lead Iodide Perovskites with organic cations: Phase transitions, high mobilities, and Near-Infrared Photoluminescent properties. *Inorg Chem* 52: 9019–9038.
45. Talmadge JM (1897) On Potassium Lead Iodid. *J Phys Chem* 1: 493–498.
46. Salau AM (1980) Fundamental absorption edge in PbI_2:KI alloys. *Sol En Mater* 2: 327–332.
47. Baltog I, Marculescu L, Mihut L (1980) Optical properties of Na:Pb single crystals. *Phys Stat Sol (a)* 61: 573–578.
48. Filip MR, Verdi C, Giustino F (2015) *GW* band structures and carrier effective masses of $CH_3NH_3PbI_3$ and hypothetical perovskites of the type $APbI_3$: A = NH_4, PH_4, AsH_4, and SbH_4. *J Phys Chem C* 119: 25209−25219.
49. Lindblad R, Bi DQ, Park BW (2014) Electronic structure of $TiO_2/CH_3NH_3PbI_3$ perovskite solar cell interfaces. *J Phys Chem Lett* 5: 648–653.
50. Repoux M (1992) Comparison of background removal methods for XPS. *Surf Interface Anal* 18: 567–570.
51. Emara J, Schnier T, Pourdavoud N (2016) Impact of film stoichiometry on the ionization energy and electronic structure of $CH_3NH_3PbI_3$ perovskites. *Adv Mater* 28: 553–559.
52. Moulder JF, Stickle WF, Sebol PE (1995) *Handbook of XPS*, Physical Electronics Inc.
53. Morgan WE, Van Wazer JR, Stec WJ (1973) Inner-orbital photoelectron spectroscopy of the alkali metal halides, perchlorates, phosphates, and pyrophosphates. *J Am Chem Soc* 95: 751–755.
54. Yeh JJ, Lindau I (1985) Atomic subshell photoionization cross sections and asymmetry parameters: $1 \leq Z \leq 103$. *Atom Data Nucl Data* 32: 1–155.
55. Giorgi G, Fujisawa J, Segawa H (2014) Cation role in structural and electronic properties of 3D organic−inorganic Halide Perovskites: A DFT Analysis. *J Phys Chem C* 118: 12176–12183.
56. Miller EM, Zhao Y, Mercado CC (2014) Substrate-controlled band positions in $CH_3NH_3PbI_3$ perovskite films. *Phys Chem Chem Phys* 16: 22122–22130.
57. Brivio F, Walker AB, Walsh A (2013) Structural and electronic properties of hybrid perovskites for high-efficiency thin-film photovoltaics from first-principles. *Appl Phys Lett Mater* 1: 042111.
58. Conings B, Drijkoningen J, Gauquelin N (2015) Intrinsic thermal instability of Methylammonium Lead Trihalide Perovskite. *Adv Energy Mater* 5: 1500477.

59. Schulz P, Edri E, Kirmayer S (2014) Interface energetics in organo-metal halide perovskite-based photovoltaic cells. *Energy Environ Sci* 7: 1377–1381.
60. Liu X , Wang C, Lyu L, et al. (2015) Electronic structures at the interface between Au and CH3NH3PbI3 in organometal trihalide perovskite-based solar cells. *Phys Chem Chem Phys* 17: 896–902.

AIMS Press